JPL D-104254 L1B
ATBD-EMIT-01

Earth Mineral dust source InvesTigation (EMIT)

EMIT L1B Algorithm: Calibrated Radiance at Sensor

Theoretical Basis

David R. Thompson, Robert O. Green, Mike Smyth
Jet Propulsion Laboratory, California Institute of Technology

Version 1.2

February 2022

Jet Propulsion Laboratory
California Institute of Technology
Pasadena, California 91109-8099

Change Log

Version	Date	Comments
0.1	July 27, 2019	Initial Draft
0.2	Sept. 29, 2019	Candidate version for peer review
0.3	Dec. 16, 2019	Changes in response to peer review
0.4	Jan 26, 2020	Added output products
1.0	April 10, 2020	Pre-CDR Science Peer Review
1.1	April 14, 2020	Orthorectification material courtesy Mike Smyth
1.2	February 2022	Updated calibration information post-TVAC2

TABLE OF CONTENTS

1. Key Teammembers

A large number of individuals contributed to the development of the algorithms, methods, and implementation of the L1b approach for EMIT. The primary contributors are the following:

- David R. Thompson (Jet Propulsion Laboratory) – EMIT Co-I, Instrument Scientist
- Robert O. Green (Jet Propulsion Laboratory) – Mission PI, Radiometric modeling
- Mike Smyth (Jet Propulsion Laboratory) – Geolocation Lead
- Michael Eastwood (Jet Propulsion Laboratory) – Calibration and Detector Technology
- Christine Bradley (Jet Propulsion Laboratory) – Optical design and Models
- Sarah Lundeen (Jet Propulsion Laboratory) – Science Data System Lead
- Randy Pollock (Jet Propulsion Laboratory – Instrument Systems Engineer

2. Historical Context and Background on the EMIT Mission and its Instrumentation

Mineral dust radiative forcing is the single largest uncertainty in aerosol direct radiative forcing (USGCRP and IPCC). Mineral dust is a principal contributor to direct radiative forcing over arid regions, impacting agriculture, precipitation, and desert encroachment around the globe. However, we have poor understanding of this effect due to uncertainties in the dust composition. Dust radiative

forcing is highly dependent on its mineral-specific absorption properties, and the current range of iron oxide abundance in dust source models (0 – 7 wt%) translates into a 460% uncertainty in regional radiative forcing predicted by Earth System Models (ESMs). Meanwhile, soil samples from North Africa regions - important sources of mineral dust - contain up to 30 wt% iron oxide. The National Aeronautics and Space Administration (NASA) recently selected the Earth Mineral Dust Source Investigation (EMIT) to close this knowledge gap. EMIT will launch an instrument to the International Space Station (ISS) to directly measure and map the mineral composition of critical dust-forming regions worldwide.

The EMIT Mission will use imaging spectroscopy across the visible shortwave (VSWIR) range to reveal distinctive mineral signatures, enabling rigorous mineral detection, quantification, and mapping. The overall investigation aims to achieve two objectives.

1. Constrain the sign and magnitude of dust-related RF at regional and global scales. EMIT achieves this objective by acquiring, validating and delivering updates of surface mineralogy used to initialize ESMs.
2. Predict the increase or decrease of available dust sources under future climate scenarios. EMIT achieves this objective by initializing ESM forecast models with the mineralogy of soils exposed within at-risk lands bordering arid dust source regions.

The EMIT instrument is a Dyson imaging spectrometer that will resolve the distinct absorption features of iron oxides, clays, sulfates, carbonates, and other dust-forming minerals with contiguous spectroscopic measurements in the visible to short wavelength infrared region of the spectrum. EMIT will map mineralogy with a spatial sampling to detect minerals at the one hectare scale and coarser, ensuring accurate characterization the mineralogy at the grid scale required by ESMs. EMIT's fine spatial sampling will resolves the soil exposed within hectare-scale agricultural plots and open lands of bordering arid regions, critical to understanding feedbacks caused by mineral dust arising from future changes in land use, land cover, precipitation, and regional climate forcing.

Data Product	Description	Initial Availability	Median Latency Post-delivery	NASA DAAC
Level 0	Raw collected telemetry	4 months after IOC	2 months	LP DAAC
Level 1a	Reconstructed, depacketized, uncompressed data, time referenced, annotated with ancillary information reassembled into scenes.	4 months after IOC	2 months	LP DAAC
Level 1b	Level 1a data processed to sensor units including geolocation and observation geometry information	4 months after IOC	2 months	LP DAAC
Level 2a	Surface reflectance derived by screening clouds and correction for atmospheric effects.	8 months after IOC	2 months	LP DAAC
Level 2b	Mineralogy derived from fitting reflectance spectra, screening for non-mineralogical components.	8 months after IOC	2 months	LP DAAC
Level 3	Gridded map of mineral composition aggregated from level 2b with uncertainties and quality flags	11 months after IOC	2 months	LP DAAC
Level 4	Earth System Model runs to address science objectives	16 months after IOC	2 months	LP DAAC

Table 1: EMIT Data Product Hierarchy

The EMIT Project is part of the Earth Venture-Instrument (EV-I) Program directed by the Program Director of the NASA Earth Science Division (ESD). EMIT is comprised of a Visible/Shortwave Infrared Dyson imaging spectrometer adapted for installation on the International Space Station (ISS). It will be installed on Flight Releasable Attachment Mechanism (FRAM) of an ExPRESS Logistics Carrier (ELC) on the ISS, in a site formally designated ELC 1 FRAM 8. NASA has assigned management of the Project to the Jet Propulsion Laboratory of the California Institute of Technology. The EMIT Payload is scheduled to be installed on the ELC 1 FRAM 8 in 2021.

Table 1 above describes the different data products to which the EMIT Mission will provide to data archives. This document describes the "Level 1B" radiometric and spectral calculations.

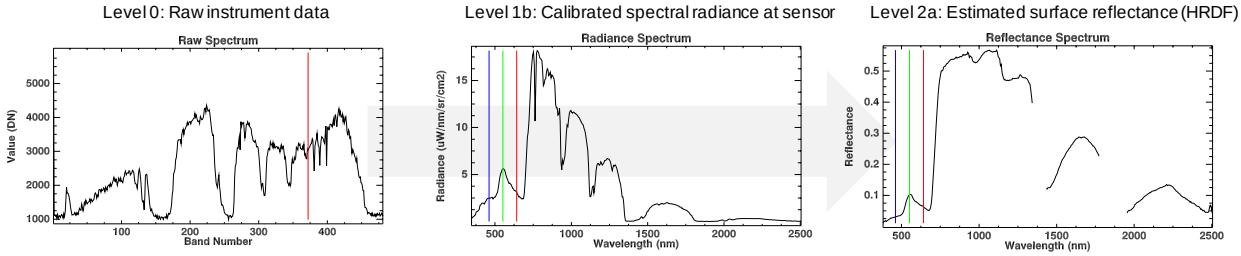

Figure 1: Representative spectra from the EMIT analysis, data product levels 0, 1B, and 2A.

This document describes the theoretical basis for the algorithm producing EMIT's calibrated "Level 1b" product, which reports spectral radiance measured at the sensor (Figure 1). It begins from reconstructed "Level 1a" products consisting of raw detector counts already recorded, downlinked, and reassembled from instrument telemetry. It then applies spectral and radiometric calibration to produce uniform radiance cubes for subsequent geolocalization. These will next be analyzed with inversion using physically-motivated surface/atmosphere models to estimate surface reflectance, the "Level 2A" product, for later analysis by mineral detection and mapping algorithms. These stages are all instantiated in the EMIT science product generation software operating at the Jet Propulsion Laboratory, California Institute of Technology. Finally, we incorporate mineral maps into Earth System modeling to evaluate Radiative Forcing (RF) impacts. Figure 2 shows a diagram of the entire workflow.

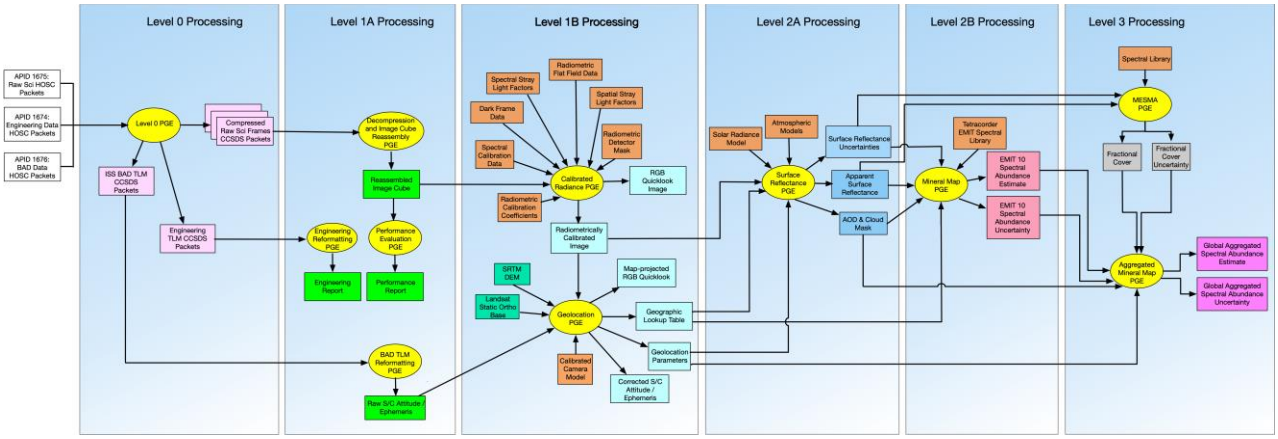

Figure 2. High-level workflow of the EMIT science data system.

3 Algorithm rationale and prior validation

The EMIT Level 1B radiometric calibration approach comes from a long history of analyses on airborne precursor instruments such as NASA's "Classic" Airborne Visible Infrared Imaging Spectrometer (AVIRIS-C, Green et al., 1998) and its next generation counterpart (AVIRIS-NG,

Thompson et al., 2017). Such analyses have been conducted in dozens of campaigns over decades of successful operations. Very similar methods have been used in prior space missions to planetary objects including NASA's M^3 Lunar exploration (Green et al., 2011) and the CRISM mission to Mars (Murchie et al., 2004).

The EMIT instrument calibration, including its noise model and various aspects of the analysis chain, does demand some specific changes due to the unique nature of the instrument. EMIT consists of a Dyson-type spectrometer with f-number 1.8, providing high optical photon throughput. It is based on a calcium fluoride refractive block, curved grating, slit, and a focal-plane array with 1280 cross track elements and 480 spectral elements, of which 328 are read from the FPA. A matched telescope contains two fixed silver mirrors for magnification. Figure 3 illustrates the optical layout by tracing ray bundles at 1440 nm. EMIT measures incident illumination at the sensor, the radiance (μm nm^{-1} cm^{-2} sr^{-1}), the "Level 1B" products from which analysts can then infer the reflectance using a model of photon transport in the atmosphere. Atmospheric correction methods vary, but the technology is sufficiently mature to provide good results over benign haze-free conditions and observing geometries (Thompson et al., 2015, 2018a, 2018b). However, high-accuracy surface reflectance estimates rest on a foundation of high-fidelity, calibrated radiance spectra (Thompson et al., 2019).

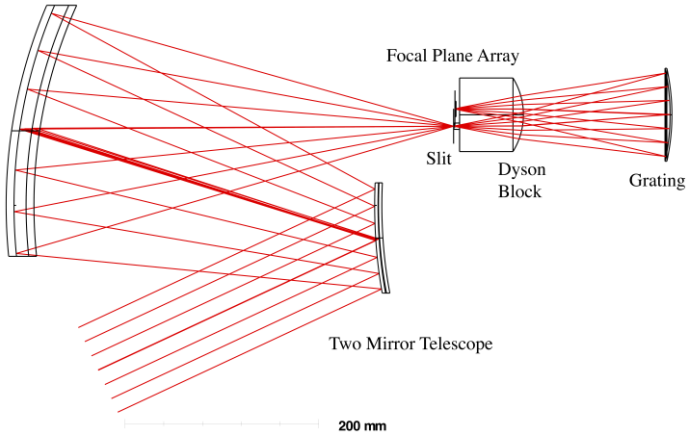

Figure 3: EMIT optical design

The system's spectral and radiometric response properties are fully-characterized in advance using laboratory measurements to provide a default calibration applicable as soon as EMIT begins operations on the ISS. Later in-flight calibration and validation (Thompson et al., 2018a, 2018b) is possible as needed, and will follow standard practice established historically by instruments such as Hyperion; it will be used to validate, and if needed, refine, laboratory calibrations.

We have generally adopted the AVIRIS-NG approach to calibration here (Chapman et al., 2019), with some minor modifications to handle the unique properties of the EMIT instrument. The geolocation technique has a similarly long heritage. It has been used for over 20 years on a wide variety of missions, including MISR, AirMISR, AirMSPI, CFIS, AFRICROM, SHIVA, OCO-3 and ECOSTRESS. ECOSTRESS also flies on the ISS, the geolocation is very similar to EMIT.

4. Algorithm description

4.1 Input data

While the EMIT input and output data products delivered to the DAAC use their formatting conventions, the system operates internally on data products stored as binary data cubes with

detatched human-readable ASCII header files. The formatting convention follows the ENVI standard, found (Jan. 2022) at https://www.harrisgeospatial.com/docs/ENVIHeaderFiles.html. The header files all consist of data fields in equals-sign-separated pairs, and describe the layout of the file. The L1B operation involves two independent operations: radiometric calibration and orthorectification, which will both be treated separately.

The specific input files needed for the L1b radiometric stage are:

1. A **dark frame** cube, derived from the temporally-closest acquisition of a dark target by the EMIT instrument, sized to the focal plane array, Band-Sequential (BSQ), with size 382x1280, in single-precision floating point. The unit is digital numbers (DNs).
2. A **DN** cube, organized in band-interleaved-by-line format, of digital numbers. The scenes can have arbitrary length but each independent frame (vertical line) of data has size 328 x 1280 and appears as 2 byte unsigned integers. The cube is arranged in Band Interleaved by Line (BIL) format.
3. A **Spectral Calibration file** provided as a 3 column ASCII file. The first column contains the channel number, the second the center wavelength, and the third the full width at half maximum. The unit is microns.
4. **Spectral Stray Light Correction Factors,** a 328 x 328 binary float 32 file, BSQ with detached ASCII header, used in the stray light PSF conditioning as described below as matrix A^+ in equation 9, and is premultiplied with the image frame to correct spectral stray response functions. These values are unitless.
5. **Spatial Stray Light Factors** file. This is the spatial analogue to 4, above. It is a matrix of size 1280 x 1280. It is used similarly to the A^+ matrix in equation 9, but it is premultiplied to the transpose of the image frame to correct spatial stray light.
6. **Radiometric Calibration Coefficients**, a 3 column ASCII file with 328 rows, providing the coefficients that transform corrected instrument digital numbers (DNs) to radiance. The unit is $\mu W\ sr^{-1}\ cm^{-2}\ nm^{-1}\ DN^{-1}$. Columns contain the channel number, calibration coefficient, and one-sigma uncertainty.
7. **Linearity Basis file,** an ENVI file with three rows and 65536 columns, in BSQ format, with a detached ASCII header, in floating point format. It describes the linearity behavior exhibited by different focal plane array elements. The first row is the mean linearity correction curve, and the remaining rows are principal components of the FPA linearity in descending order of significance. For each linearity correction curve, the column index represents the digital number associated with the uncorrected radiometry. The value itself is the unitless coefficient multiplied by the measurement to obtain its corrected version.
8. **Linearity Map,** a 328 x 1280 x 2 ENVI file representing the basis coefficients for each pixel. To recover the linearity curve for an individual pixel, simply multiply the coefficients by their associated principal component basis functions and add the mean.
9. **Radiometric Flat Field** file, the flat field coefficients which indicate the relative radiometric response of each focal plane array element, as described below. These coefficients are stored as an image the same size as the focal plane array, a 328 x 1280 x 2 channel binary float 32 file, BSQ with detached ASCII header. The first channel contains the unitless flat field value, and the second channel contains the one-sigma uncertainty on this value.
10. **Bad Element Mask**, a single 16 bit signed integer frame, with detatched ASCII header, containing information about the location of known bad pixels. Zero indicates good pixels. <1 indicates bad pixels and number of contiguous bad pixels in the spectrum. >1 indicated row and column masked pixels. For more information on how this file is used, we refer the reader to Chapman et al (2019).

11. **Spatial Ghost Map**, a .json file that describes the positions and magnitudes of spatial ghosts, which are unwanted reflections that cause stray features on the EMIT FPA. These are used by the radiometric calibration code to estimate and remove the ghost contribution. The format a hierarchical dictionary, with the top level holding data about the features that are common to all ghost features, and then a list of "orders" describing the specific parameters of each feature.

The input files needed for the L1b geolocation stage are:

1. **Raw Spacecraft Attitude and Ephemeris,** a L1A product. Contains the uncorrected Broadcast Ancillary Data (BAD) ephemeris and attitude quaternions from the ISS.
2. **Raw Line Time,** a L1A product. Contains the collection time for each line of data.
3. **Calibrated Geometric Camera Model**, a text file contains a description of the camera. Generated based on pre-flight measurement and early mission calibration.
4. **Surface Radar Topography Mission (SRTM) DEM**, a global 30m digital surface model. Based on NGA/NASA SRTMv3 height files, with voids filled in using ASTERv2 data.
5. **Landsat 7 orthobase**, a global ortho-rectified Landsat dataset. Mostly cloud-free. Resolution depends on the band, Landsat bands 1-5 and 7 are 28.5 meter, band 61 and 62 are 57.0 meter and panchromatic band is 14.25 meter.

Table 2 Below enumerates all products.

Radiometry Input file	Format	Interpretation	Notes
Radiometric Dark Level	328 x 1280 binary 32 bit floating point, BSQ interleave with detached ASCII header	Offset value to be subtracted from each element before radiometric analysis.	From unilluminated portion of orbit.
DN	328 x 1280 x N binary 16 bit unsigned integer, BIL interleave with detached ASCII header	Instrument observation data (L1a)	One scene of instrument record data from the L1a product.
Spectral Calibration File	Three channel ASCII file	Channel, center wavelength, and FWHM in microns	Spectral calibration
Spectral Calibration Matrix	328 x 1280 x 2 binary 32 bit floating point, BSQ interleave with detached ASCII header	Matrix version of the spectral calibration file. Channels show center wavelength and FWHM in microns at each FPA pixel.	
Spectral Stray Light Factors	328 x 328 binary 32 bit floating point, BSQ, detached ASCII header	Correction matrices as in Chapman et al. (2019)	Brings response functions towards Gaussian
Radiometric Calibration Coefficients	Three column ASCII file	Channel, uW /cm^2 / nm / sr / DN, and one-sigma uncertainty	Maps DN to radiance
Linearity Basis File	3 x 65536 binary 32 bit floating point, BSQ interleave with detatched ASCII header	Mean and two principal components of linearity behavior	
Linearity Map	328 x 1280 x 2 binary 32 bit floating point, BSQ interleave with detatched ASCII header	Principal component coefficient values describing linearity behavior of each FPA element	
Radiometric Flat Field	328 x 1280 x 2 binary 32 bit floating point, BSQ, detached ASCII header	Small relative radiometric corrections that refine the RCC-predicted radiance value. Should be close to unity. With uncertainties in second channel	Fine correction of radiometric coefficient. Nominally from pseudoinvarient targets.
Bad Pixel Mask	328 x 1280 binary 16 bit integer, BSQ, detached ASCII header	Zero indicates good pixels. <1 indicates bad pixels and number of contiguous bad pixels in the spectrum. >1 indicated row and column masked pixels.	From laboratory calibration measurements. Updated as needed.
Spatial Stray Light Factors	1280 x 1280 binary 32 bit floating point, BSQ, detached ASCII header	Correction matrices as in Chapman et al. (2019).	Brings response functions towards Gaussian
Spatial Ghost file	.JSON file	Configuration of spatial ghost model	

Geolocation input file	Format	Interpretation	Notes
Raw Spacecraft Altitude and Ephermeris	NetCDF	Uncorrected Broadcast Ancillary Data (BAD) ephemeris and attitude quaternions from the ISS.	
Raw Line Time	NetCDF or CSV (TBD)	Collection time for each line of data.	
Calibrated geometric camera model	XML	Text file description of the camera, generated from pre-flight measurement and on-orbit checkout calculations	
Surface Radar Topography Mission (SRTM) Digital Elevaiton Model (DEM)	VICAR format	A global 30m digital surface model based on NGA//NASA SRTMv3 height files, with voids filled using ASTER v2 data.	
Landsat 7 orthobase	VICAR format	A global ortho-rectified Landsat dataset. Mostly cloud-free. Resolution depends on the band, Landsat bands 1-5 and 7 are 28.5 meter, band 61 and 62 are 57.0 meter and panchromatic band is 14.25 meter.	

Table 2: Input files

Further information on the development of these values appears in the calibration section below.

4.2 Theoretical description of radiometric and spectral calibration

While the EMIT instrument was designed to optimize uniformity and spectroradiometric accuracy, all physical instruments suffer some degree of systematic distortion. Incoming light is modified by various imperfections in the EMIT optics before being cast onto the focal plane array. Then, the focal plane has its own unique electronic fingerprint on the DN data stream. The overall goal of electronic and optical corrections is to produce the FPA response that would have been observed by an "ideal" instrument, i.e., one having perfect Gaussian spectral response functions and perfectly linear radiometry. In practice, this involves multiple steps which work backwards to reverse the electrical and optical distortion processes. The following sections describe each step in greater detail.

Fundamentally, the conversion from DNs to measured radiance L_{FPA} uses a proportional relationship:

$$L_{fpa}(r,c) = f(D_0, r, c)\ \beta(r,c)$$
$$D_0 = D(r,c) - \alpha(r,c) \quad (1)$$

Where D_0 is the zero-point-corrected digital number readout from the focal plane array, and the radiance $L_{FPA}(r,c)$ is a function of row r and cross-track spatial location c. The nonlinear function f corrects nonlinearities in the detector response, so that radiance becomes directly proportional to DNs and the gain factor $\beta(r,c)$ can be treated as having units of $\mu W\ nm^{-1}\ cm^{-2}\ sr^{-1}\ DN^{-1}$. The term $\alpha(r,c)$ represents the zero-point offset, which is also measured in Digital Numbers (DNs).

Dark frame subtraction. The first step of calibration is to estimate the zero point of the EMIT focal plane array, given by $\alpha(r,c)$. The zero point represents the value that each FPA element reports when it is not illuminated. It can be further decomposed into an additive combination of two contributions:

$$\alpha(r,c) = \alpha_{dark}(r,c) + \alpha_{ped}(r,c) \quad (2)$$

Here $\alpha_{dark}(r,c)$ corresponds to the dark current and detector bias, which varies over minute timescales, and $\alpha_{ped}(r,c)$ corresponds to a distortion known as the pedestal shift, which is more structured but is different for each integration. In orbit, we estimate $\alpha_{dark}(r,c)$ by acquiring a data sequence from the

dark side of the Earth, and combining these integrations to form a temporal average called a "dark frame" of values at zero illumination. For laboratory data, a non-illuminated scene is used instead.

Pedestal shift correction. Electronic effects can also cause individual rows and columns to shift their zero points independently on much shorter timescales. This phenomenon includes electronic artifacts known as pedestal shift. To remove these differences, we analyze the values in non-illuminated rows and columns at the periphery of the focal plane array. These rows and columns are covered with a blocking filter, and are known to be fully dark. For each row we average the non-illuminated pixels in the masked columns on either side, and then remove the residual zero offset. We then perform the same operation in along each column, based on the masked rows of the FPA. We calculate each FPA element's pedestal shift $\alpha_{ped}(r,c)$ via:

$$\alpha_{ped}(r,c) = \frac{1}{|M|}\sum_{m\in M}[D(r,m) - \alpha_{dark}(r,m)] + \frac{1}{|N|}\sum_{n\in M}[D'(n,c) - \alpha_{dark}(n,c)] \quad (3)$$

Here M is the set of masked columns, and N is the set of masked rows. A prime symbol D' is used to indicate that these FPA elements have already received a column-wise pedestal shift correction. This completes the zero point estimation.

Bad pixel replacement. The EMIT focal plane array, like most detectors, contains isolated pixels or clusters of pixels with a response that differs significantly from their neighbors. Some do not respond at all. While the number of these bad pixels is small — less than 0.1% of the total — the single-channel artifacts they create are obvious in data statistics and derived products. We identify these bad pixels at commissioning through the traditional method of using a flat field measurement produced with a uniformly illuminated spatially-uniform calibration object, such as an integration sphere. We flag outlier pixels by thresholding their standard deviations, and then augment the list manually with a handful of pixels that escape manual detection. In typical HgCdTe detectors like that of EMIT, the resulting bad pixel list remains stable after commissioning.

While bad pixels are only cataloged once, they must be corrected independently in each image frame using a statistically appropriate interpolation (Chapman et al., 2019). Simple linear interpolation in the spectral dimension is inadequate, since it does not respect the channel- wise structure of real spectra; it distorts the underlying data statistics for downstream analyses. Instead, we exploit the spectral shapes of nearby locations that are similar to the spectrum undergoing correction. Given a spectrum s' with bad pixels, we identify the most similar spectrum in its image frame, s^*, and then fit a linear relationship between the radiance values of s^* and s'. Similarity between spectra is defined by the spectral angle:

$$\mathbf{s}^* = \mathrm{argmin}_s \frac{\langle \mathbf{s}', \mathbf{s} \rangle}{|\mathbf{s}'|_2 \ |\mathbf{s}|_2} \quad (4)$$

After identifying s^*, we predict the missing values in the incomplete spectrum by fitting a linear regression model that maps spectral points of s^* onto the incomplete spectrum s', minimizing least squares error with standard closed-form expression. Naturally, we exclude the bad channels from this calculation. We then apply the map to predict the missing values in s'.

Filter Seam Interpolation. There is one exception to the bad pixel replacement rule. EMIT uses a series of order sorting filters to reject the higher orders of the dispersed light from the grating. One filter boundary lies at 1290 nm, and it often creates single-pixel anomalies and high noise values at this specific channel. To avoid this, we interpolate linearly across this channel everywhere in the FPA. Since it lies at the edge of a deep water vapor absorption feature, this single channel is not likely to be critical for any EMIT science objective.

Linearity Correction. The EMIT FPA elements are not perfectly linear in their response to increasing illumination; typical elements depart by about 1% from perfect linearity. However, different FPA elements have different linearity curves. To fully characterize their performance, we test their response using a variable-aperture integrating sphere with a mechanical closure that changes the illumination intensity reaching the sensor. A photodiode installed in the sphere reports an intensity value that is believed to be more linear than EMIT's HgCdTe array. We calculate the ideal linearized value for each photodiode level using a linear fit with photodiode readings as the abscissa and the EMIT reported DN values as the ordinate. We then calculate the fractional change in value which maps each FPA onto its ideal. This provides a linearity correction curve which is close to unity, but varies across the dynamic range.

The linearity correction curves are different for all FPA elements. We reduce this variance using principal component analysis, recording only the mean and first two principal components for each curve. This means that we can describe the unique linearity correction curve using just two numbers, which are stored together in a two-channel linearity coefficient map having the same dimensions as the focal plane array. At runtime, the linearity curve is reconstructed so that the desired correction can be applied. For each pixel, we define a linearity correction vector T of length 2^{16}, with elements from 0 to 65535 inclusive. The value stored at each element is the coefficient which multiplies that digital number in order to linearize the detector response. We define the function T(DN,r,c) as this lookup operation, so that – for example - T(500,r,c) is the coefficient which multiplies a digital number output of 500 from row position r and column c in order to linearize the detector response at that FPA element. For an uncorrected spectrum, in row r and column c, the linearity vector T is given by:

$$T(DN, r, c) = ak_1(r, c) + bk_2(r, c) + \mu$$
$$f(DN, r, c) = T(DN, r, c)\ DN \quad (5)$$

Where a and b are the first two principal component basis vectors, μ is the mean nonlinearity, and k_1 and k_2 are the PCA basis coefficients that are different for each row and column.

Flat Fielding. The gain term $\beta(r,c)$ in Equation 1 is a radiometric calibration coefficient (RCC) and can be further decomposed into the multiplicative form:

$$\beta(r, c) \ = \ \beta_{rcc}(r)\ \beta_{flat}(r, c) \quad (9)$$

where $\beta_{RCC}(\lambda)$ is the spatially independent calibration coefficient and $\beta_{flat}(r,c)$ is the spatially varying flat field. Here we note that the average flat field value in each spectral channel, that is the average of all cross track positions, is constrained to unity:

$$1 \quad = \quad \left[\frac{1}{|C|}\sum_{c\in C}\beta_{flat}(r, c)\right] \quad \forall r \quad (10)$$

Infield Stray Light Correction. The measured radiance $L_{apt}(\lambda)$ represents the best estimate of light at the detector using the nominal Gaussian line shape which is measured in the laboratory. However, any physical instrument exhibits some degree of non-Gaussian response behavior. These perturbations often take the form of "thick tails" to the response function; even at levels which are three or four orders of magnitude below the peak, they can reduce the spectral contrast of features such as sharp atmospheric absorptions (Thompson et al. 2018). Such distortions arise because, in practice, each incoming ray is partially scattered through interactions with different areas of the optical system and the scattered light ultimately propagates onto multiple areas of the detector array. These unwanted signals cause spatial and spectral blurring within the scene.

After standard radiometric calibrations, we estimate the stray spectral response function as described in Thompson et al. (2018). We begin by defining a matrix representing the incoming at-aperture radiance for a large number of wavelengths d, where $d \gg 328$, at each of the 1280 cross-track locations, and write it as L_A. The Gaussian nominal spectral response function is represented by a linear operator H of size $328 \times d$. We posit a vertical stack of single spectral response functions per output channel can transform the true at-aperture radiance, L_A, into the apparent radiance L_N:

$$\mathbf{L_n} = \mathbf{H}\mathbf{L_A} \tag{6}$$

Here, for convenience, we represent a frame of radiance data using boldface vector notation, with capital letters representing matrices. Due to the fact that the matrix **H** has a rank less than d, the nominal spectral response function is not invertible and it eliminates spectral details finer than the instrument's ideal resolution. The resultant nominal response L_N contains dimensions of a data frame, a 328×1280 matrix with 328 spectral channels and 1280 cross-track positions.

The measured response $\mathbf{L_M}$ can be modeled by distorting the nominal response L_N by some stray spectral response, modeled for convenience as a 328x328 linear operator G. In addition, a small Gaussian random variable ε is added, which combines the read noise, dark noise, and photon shot noise in quadrature. This allows the following operations:

$$\begin{aligned}
\mathbf{L_M} &= \mathbf{G}\mathbf{H}\mathbf{L_A} + \mathbf{H}\mathbf{L_A} + \epsilon \\
\mathbf{L_M} &= \mathbf{G}\mathbf{L_N} + \mathbf{L_N} + \epsilon \\
\mathbf{L_M} &= [\mathbf{G} + \mathbf{I}]\mathbf{L_N} + \epsilon \\
\mathbf{L_M} &= \mathbf{A}\mathbf{L_N} + \epsilon
\end{aligned} \tag{7}$$

where A corresponds to the stray spectral response operator with an identity matrix added along it's diagonal, as performed in prior work by Zong et al. (2006). We define a correction operator to recover the nominal data frame which would have been found under the nominal spectral response function by inversion of the stray spectral response functions influence. The Moore-Penrose pseudoinverse $\mathbf{A^+ = (A^T A)^{-1} A^T}$ guarantees $\mathbf{A{+}A = I}$. The resulting most probable unperturbed measurement $\hat{\boldsymbol{L}}$ is:

$$\hat{\mathbf{L}} = \mathbf{A}^{+}\mathbf{L_m} \tag{8}$$

We perform this operation independently in both spatial and spectral dimensions. This limits the correction to blurring functions that are separable, i.e. representable as independent operators applied sequentially in the spatial and spectral dimensions. This is not an onerous constraint in practice and we find that families of Gaussian distributions and other isotropic or separable functions are a sufficient palette to represent Point Spread Function (PSF) broadening effects.

Ghost Correction. The EMIT spectrometer experiences an optical ghost caused by an unwanted reflection from the order sorting filter. This unwanted optical path returns to the opposite side of the focal plane array, causing a spatially-symmetric pattern. However, the spectrum of the ghost reflection is a distorted version of the original. This artifact is typically 1% or less of the total energy incident on the FPA, but it is still significant for relative spectroscopic measurements so the EMIT spectroradiometric calibration attempts to model and correct it.

The ghost correction for a single frame of data involves two parts. First, we build a predicted ghost frame that would have been caused by the given scene. We then subtract the ghost frame from the original to produce a corrected image. This is slightly inaccurate because the original scene from which the ghost frame was estimated itself included some ghost signal, which would be . However, this inaccuracy is no greater than the relative magnitude of the ghost itself, which is less than 1%, and greatly simplifies calculations.

Our ghost model maps each wavelength of the source onto a different wavelength on the opposite side, reflecting about a known axis of symmetry near the center of the focal plane array. The mapping of source to ghost wavelengths appears in Figure 4 below. Each line in the leftmost plot is an "order" that is further subdivided into segments represented by lines in (channel, channel) space. Each segment has an intensity profile that indicates the ratio of source radiance to ghost radiance. This intensity profile is also linear in the source wavelengths; it is represented by a slope and offset. Finally, we apply a spatial blurring kernel to the ghost image to capture the additional scatter induced by optical components along the ghost path. This blurring operator uses a lineshape defined independently for different wavelength regions, where each region's point spread function is formed from concentric Gaussian distributions with distinct widths and intensities. These blurring operators are optimized to remove the ghost image using laboratory test data.

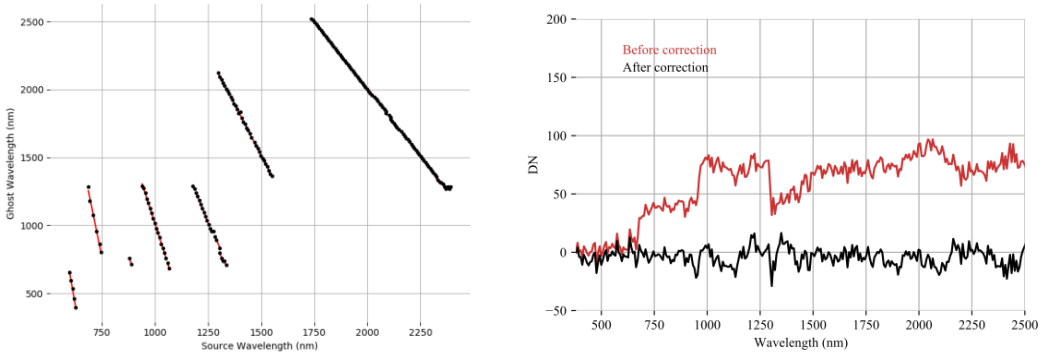

Figure 4: (Left) Wavelength map describing source/ghost relationships. (Right) Ghost spectrum, before and after correction.

Wavelength Calibration. In the final step of spectroradiometric calibration, we apply a wavelength assignment. Our initial solution uses monochromatic laser sources of known wavelengths used in laboratory characterization measurements, which then feed a linear wavelength calibration model. If needed we refine the initial wavelength calibration after operation begins with flight data using a single uniform shift to match atmospheric absorption features in the top of atmosphere (TOA) reflectance spectrum. This procedure uses the ISOFIT codebase for atmosphere surface estimation (https://github.com/isofit/isofit), which implements a Bayesian Maximum A Posteriori approach described in Thompson et al., (2018). In addition to the standard state vector elements handling surface and atmosphere parameters, we use an extra state vector element corresponding to the wavelength shift. A more complete description of our atmosphere estimation code appears in the EMIT L2A ATBD.

4.3 Theoretical description of geolocation

The EMIT instrument is a Dyson-type spectrometer. As the ISS moves forward, the push broom sample the ground in the along-track direction.

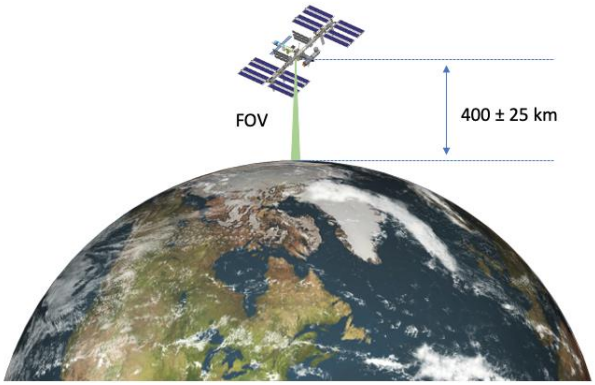

Figure 6: EMIT Collection

The instrument has 328 channels in the spectral direction, with 1280 cross track elements. The instrument has a focal length and pixel pitch given in the table 3. A line of data is collected every 9.26 ms.

Camera parameter	Value
Spectral Channels	328
Cross Track Elements	1280
Time between lines	9.26 ms
Focal Length	193.5 mm
Pixel Pitch X direction (cross track)	30 micron
Pixel Pitch Y direction (along track)	30 micron
Cross track FOV	± 5.52°
Cross-track IFOV	155 microradians
Along-track IFOV	171 microradians

Table 3: Camera parameters

From the 400±25-km ISS altitude, the resulting swath is 80 km wide, and a pixel footprint size of approximately 62m x 68m. In general, a spectrometer may have channels separated on the surface, and may have a varying spectral response for different cross track errors. The channel co-registration correction is called “keystone”, and the spectral response correction is called “smile”. However, for EMIT the 328 channels are close to coincident on the surface and the center channel of the spectral response across the cross track elements is nearly constant (within 2%). So there is no significant “keystone” or “smile” to correct for EMIT. The instrument is curved in the cross track direction, as shown in Figure 5.

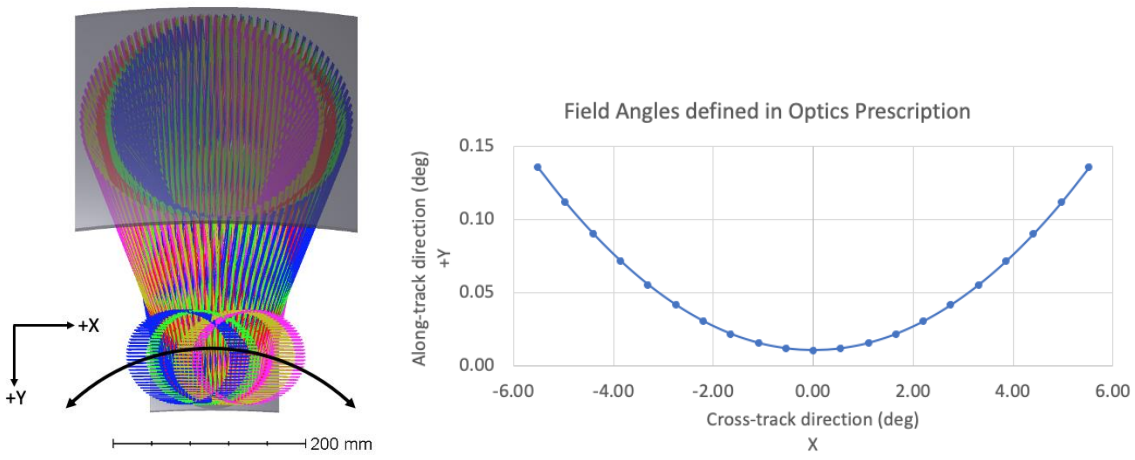

Figure 5: Cross track curvature

The acquisition strategy for EMIT is to collect 3-12 flight paths per orbit and can vary in length by 15 seconds (~1620 lines) to 570 seconds (~61,560 lines). 90% are < 180 sec. The data is broken into fixed size scenes of 1280 lines, with any extra lines in a flight path going into the final scene which will be between 1280 and 2559 lines.

Geolocation Approach

Geolocation is derived by propagating the instrument pointing model from the payload on the Express Logistics Carrier (ELC) 1 Flight Releasable Attachment Mechanism (FRAM) 8 (or ELC 1 FRAM 8) it is mounted on, to the different ISS elements, until it is intersected with the ground topography. The pointing model provides a mapping from image pixel (u, v) and time t to a look vector $\vec{L}_{ECEF}$ in ECEF coordinates. $\vec{L}_{ECEF}$ is a unit vector that points in the direction the image pixel (u, v) looks. Given $\vec{L}_{ECEF}$ along with the position $\vec{P}_{ECEF}$ of the spacecraft we can then calculate the ground location viewed at a given height. The mapping from (u, v, t) to $\vec{L}_{ECEF}$ and $\vec{P}_{ECEF}$ occurs in a number of steps:

$$\vec{L}_{ECEF} = T^{t}_{ISSAC\ to\ ECEF} \circ T_{Payload\ to\ ISSAC} \circ T_{ICS\ to\ Payload}(\vec{L}_{ICS}(u, v))$$
$$\vec{P}_{ECEF} = T^{t}_{ECI\ to\ ECEF}(\vec{P}_{ECI}(t))$$

The camera model data is used to generate a look vector $\vec{L}_{ICS}$ for a given image pixel (u, v). The EMIT Optics Detector Coordinate Frame is shown in Figure 6.

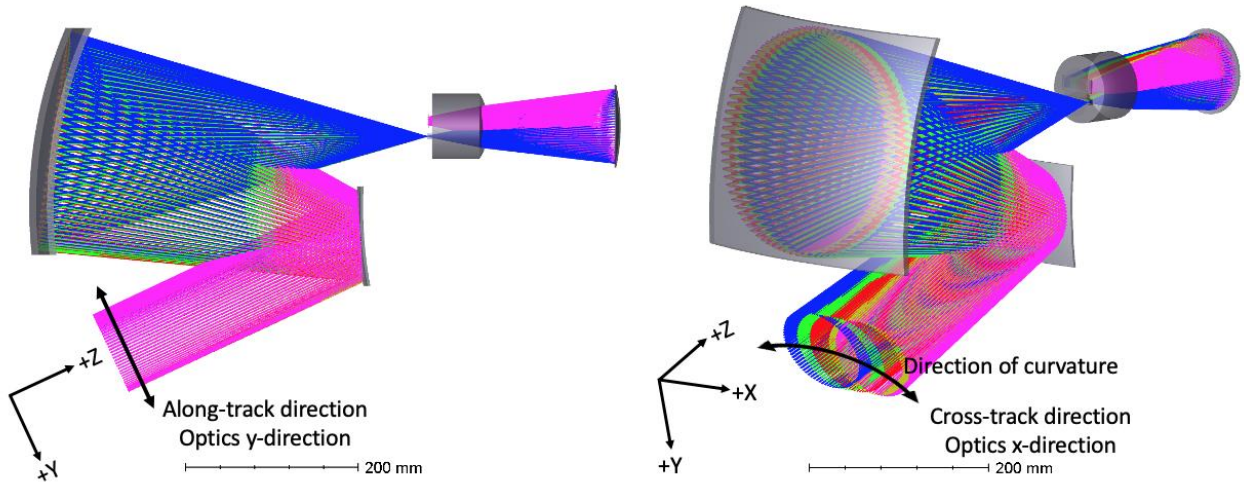

Figure 6: Optics coordinate system

We start in the detector coordinate system (DCS) which lies in the plane of the focal plane with x-axis in the cross track column or u direction, y-axis in the along track row or v, and z-axis perpendicular to the focal plane. For a strictly linear camera model we can model this as a pinhole camera, giving us:

$$\vec{L}^{Pinhole}_{DCS}(u, v) = \begin{bmatrix} (u - u_p)p_u \\ (v - v_p)p_v \\ -f \end{bmatrix}$$

Here the principal point $(u_p . v_p)$, pitch (p_u, p_v) and focal length f come from the camera model. We modify this simple pinhole model to include the curvature of the grating (TBD, description of using field angle map). By convention, we scale this to a unit vector:

$$\vec{L}_{DCS}(u,v) = \frac{\vec{L}_{DCS}^{unscaled}(u,v)}{\left\|\vec{L}_{DCS}^{unscaled}(u,v)\right\|}$$

We then rotate this to the instrument coordinate system (ICS), again using information from the camera model, $T_{DCS\ to\ ICS}$:

$$\vec{L}_{ICS}\ (u,v) = T_{DCS\ to\ ICS}(\vec{L}_{DCS}(u,v))$$

We then rotate this to the instrument coordinate system (ICS), again using information from the camera model, $T_{DCS\ to\ ICS}$: It is common that the instrument and payload axes may not be exactly aligned and that small boresight angles may need to be calibrated during the initial flight calibration. Then defining a 3D rotation matrix R_{boresight} accounting for boresight angles can be defined so that the calibrated model accounts for the difference in alignment.

$$T_{DCS\ to\ ICS}^{Calibratied} = R_{boresight} T_{DCS\ to\ ICS}^{Uncalibrated}$$

Figure 7 shows the orientation of ExPRESS logistics carrier (ELC) EMIT is located on the ELC 1 FRAM 8.

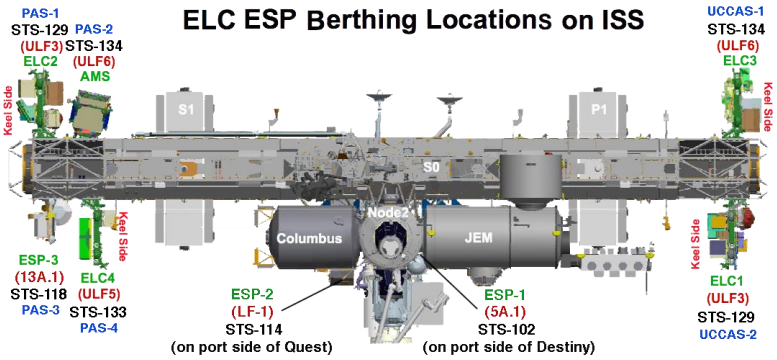

Figure 7: Location of ELC and ESPs on the ISS (NASA - NASA STS-129 Press Kit)

The payload coordinate system is shown in Figure 8.

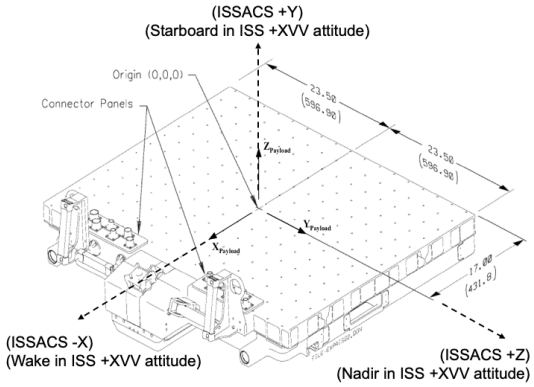

Figure 8: Payload Coordinate System

We can express the change of coordinates form the instrument reference frame to the payload reference frame as:

$$\begin{bmatrix} X_P \\ Y_P \\ Z_P \\ 1 \end{bmatrix} = \begin{bmatrix} 1 & 0 & 0 & 0 \\ 0 & 1 & 0 & 0 \\ 0 & 0 & 1 & 0 \\ 0 & 0 & 0 & 1 \end{bmatrix} \begin{bmatrix} X_{ICS} \\ Y_{ICS} \\ Z_{ICS} \\ 1 \end{bmatrix}$$

Figure 9 defines the ISS fixed body axis.

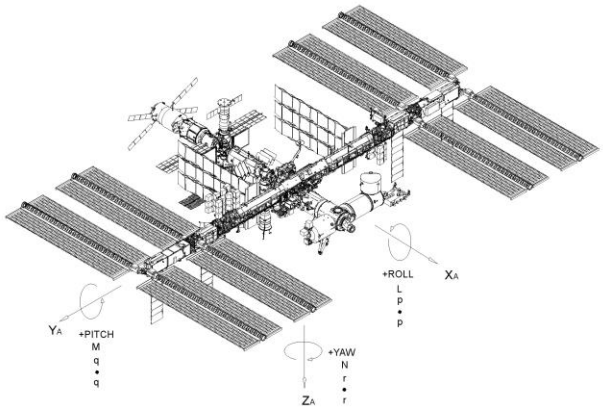

Figure 9: ISS Analysis Coordinate System from "ISS coordinate systems" (2008)

The change of reference frame between the FRAM and the ISS fixed body reference frame is:

$$\begin{bmatrix} X_A \\ Y_A \\ Z_A \\ 1 \end{bmatrix} = \begin{bmatrix} 1 & 0 & 0 & x_A^0 \\ 0 & 1 & 0 & y_A^0 \\ 0 & 0 & 1 & z_A^0 \\ 0 & 0 & 0 & 1 \end{bmatrix} \begin{bmatrix} X_P \\ Y_P \\ Z_P \\ 1 \end{bmatrix}$$

The center of the payload reference frame in the ISS fixed body frame is given by (supplied by Email request to CAMMP group) (TBD – Trace through coordinate systems and check that this is right):

$$\begin{cases} x_A^0 = -81.82\ in = -2.0782\ m \\ y_A^0 = -919.27\ in = -23.3495\ m \\ z_A^0 = 281.14\ in = 7.1410\ m \end{cases}$$

Attitude of the ISS is given as Euler angles between the ISS orbital reference system (also called LVLH for "Local Vertical Local Horizontal") and is described in Figure 10.

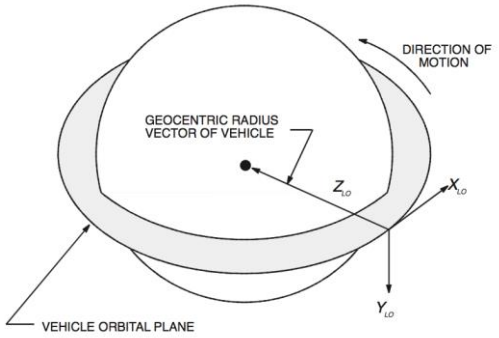

Figure 10: Orbital reference system definition ("ISS coordinate systems", 2008)

Attitude rotation matrices for roll, pitch, and yaw angles are given by:

$$R_{pitch} = \begin{bmatrix} \cos(p) & 0 & \sin(p) \\ 0 & 1 & 0 \\ -\sin(p) & 0 & \cos(p) \end{bmatrix} R_{roll} = \begin{bmatrix} 1 & 0 & 0 \\ 0 & \cos(r) & -\sin(r) \\ 0 & \sin(r) & \cos(r) \end{bmatrix} R_{yaw} = \begin{bmatrix} \cos(y) & -\sin(y) & 0 \\ \sin(y) & \cos(y) & 0 \\ 0 & 0 & 1 \end{bmatrix}$$

From Figure 14, we define the orbital reference frame (LVLH) axis as:

$$\begin{cases} \vec{Z}_{LVLH}(t) = -\dfrac{\vec{P}(t)}{\left\|\vec{P}(t)\right\|} \\ \vec{Y}_{LVLH}(t) = \dfrac{\vec{Z}(t) \times \vec{V}(t)}{\left\|\vec{Z}(t) \times \vec{V}(t)\right\|} \\ \vec{X}_{LVLH}(t) = \vec{Y}(t) \times \vec{Z}(t) \end{cases} \qquad (1)$$

Where *P(t)* is the ISS position at time *t* expressed in Earth-centered inertial (ECI) and *V(t)* corresponds to the ISS velocity vector at time *t*, expressed in ECI. Then, we can express the change of reference frame from the Orbital to the ECI reference frame with the matrix:

$$M_{Orb2CTRS} = \begin{bmatrix} X^x_{LVLH} & Y^x_{LVLH} & Z^x_{LVLH} & 0 \\ X^y_{LVLH} & Y^y_{LVLH} & Z^y_{LVLH} & 0 \\ X^z_{LVLH} & Y^z_{LVLH} & Z^z_{LVLH} & 0 \\ 0 & 0 & 0 & 1 \end{bmatrix} \qquad (2)$$

Spacecraft position is given in Earth-centered inertial (ECI) coordinates. This is the same as the J2000 celestial reference frame. It's North pole or Z axis is along the predicted rotation vector of the Earth at midnight, Jan 1, 2000 AD (JD 2451545.0); its X axis is toward the vernal equinox on that date, and it's Y axis comprises a right handed orthonormal triad with the X and Z axes, in the order X,Y,Z. This frame is nearly inertial; its origin has a small acceleration (~ 0.5 cm/s2) because the Earth goes around the sun, but its axes remain aligned with an inertially fixed set of directions. For geolocation, we need to convert to Earth-Centered Earth-Fixed (ECEF), also known as ECR ("Earth-Centered Rotational). This gives position in meters. The point (0,0,0) is at the center of the earth, Z-axis goes through true north (which is not the same as the instantaneous earth rotational axis). X-axis intersects the earth at 0 latitude, 0 longitude, and Y-axis completes the right handed coordinate system. These conversions are handled by standard toolkit libraries, see (Noerdlinger, 1995) and ("SPICE Toolkit Reference Frames", 2019). These account for:

1. Precession of Earth's axis. This is the motion of north rotation pole about the ecliptic pole (long term change, due to torques of sun and moon on earth)
2. Nutation of Earth's axis (same source as precision, but shorter term – conventionally the full precession is separate into long and short term components).
3. Axial rotation based on UT1 (Diurnal Earth rotation, including small corrections in the earth rotation rate, unaccounted for can result in as large as 450 meter error)
4. Polar motion. This is small motion of the earth's crust in relation to its rotation as a solid body. This is an about 10 meter correction.

In addition, there are several corrections to consider:

1. Aberration of Light
2. Light travel time
3. Atmospheric refraction

Aberration of light is change in view direction due to the relative motion of the spacecraft with earth. This is exactly the same as the apparent movement of stars due to stellar aberration, just pointed downward. This is effect is proportional to v/c and is about 5 arcseconds for Low Earth Orbiting spacecraft (LEO). The result on the ground depends on the viewing geometry, but can be 40 meters or so. For a unit look vector, this correction is:

$$\vec{u}_{corr} = \vec{u}_{rest\ frame} + \frac{\vec{v}}{c}$$

Light travel time accounts for the difference that light leave the surface at one time t_1, but the spacecraft has moved when the light arrives at time t_2. This is a small effect for LEO, on the order of 3 meters or so. We ignore this effect. Atmospheric refraction affects the view angle from a spacecraft. This can be important for steep viewing angles, but for moderate viewing angles (e.g., up to 45 degrees zenith) the displacement is on the order of 5 meters (see (Noerdlinger, 1995) for a discussion of this). We ignore this effect.

We have the expression combining the look vector for image coordinate (u, v) with the position at time t for a distance λ along the look vector of:

$$\vec{X}(t, u, v) = \vec{P}_{ECEF}(t) + \lambda \vec{L}_{ECEF}(t, u, v)$$

To determine the geolocation with the Earth ellipsoid with elevation h, we determine λ such that X is at the intersection of this ray with the ellipsoid:

$$\frac{X_x^2 + X_y^2}{A^2} + \frac{X_z^2}{B^2} = 1$$

Using the WGS-84 ellipsoid, we have

$$\begin{cases} A = a + h \\ B = b + h \end{cases} \quad \text{with} \quad \begin{cases} a = 6378137m \\ b = 6356752.3142m \end{cases}$$

The equation can be expanded as a second order polynomial and solved. Two solutions will be obtained, the smallest one being the one we are looking for (the other one is the intersection with the other side of the Earth's ellipsoid). Note that we can easily determine the inverse, given a point on the surface we can determine (u, v) by using a standard root finder. Also, as mentioned above, we can easily determine the inverse, given a point on the surface we can determine (u, v) by using a standard root finder. We can include the height term in the location of the surface, as determined by our DEM.

ISS Stability Analysis

The previous section detailed how the geolocation of a given pixel can be determined given the instrument characteristics, the ISS positions, velocities, and attitude angles, and geolocation accuracy therefore directly depends on the accuracy of these parameters. In the following paragraphs we explore the impact of the ISS position and attitude angles uncertainties on the geolocation uncertainties. The attitude rate error for the ISS is expected to be 0.001deg/second per axis (3 sigma).

At a height of 400 km this is 2.3 m per second relative geolocation error. At any given time, the ISS on-board instrument are expected to deliver attitude data with 3-sigma uncertainty better than 1 deg/axis for any instrument attached to the ISS (Gomez, 2015). Considering 1/3 deg/axis maximum uncertainty at any given time, the geolocation error becomes 2.5 km at 1-sigma in absolute geolocation error. The ISS position uncertainty is given at 45.8m at 1-sigma. The image time stamp has a time uncertainty of 1 ms (TBD – replace with actual EMIT timing error). The ISS velocity is approximately 7 km/s, so a 1 ms error is approximately 7m geolocation error.

This stability analysis indicates that geolocation uncertainties during the acquisition of a given scene are negligible and likely account for a fraction of the image pixel size. We conclude that the relative geolocation accuracy of EMIT imagery is expected to be meet all requirements. However, it was also shown that absolute orientation accuracy could suffer due to inaccurate absolute knowledge of the ISS attitude angles. This uncertainty will introduce an absolute geolocation uncertainty of 2.5km at 1-sigma. ECOSTRESS has been collecting information about the initial uncorrected geolocation errors, and the final corrected geolocation errors since July 2018. This data should be representative of the geolocation errors we expect for EMIT. The data is show in Figure 11 and 12, and summarized in Table 2. As can be seen from the data, one standard deviation ISS geolocation error is 1.3 km, that is then corrected to 46.9 m.

This analysis of the geolocation uncertainties indicates that the primary source of error could be attributed to lack of knowledge of absolute attitude angles. However, relative attitude information is known with sufficient accuracy that the corresponding geolocation error should account for less than a fraction of the EMIT pixel size. Therefore, at the time-scale of a given scene, accurate absolute geolocation can be achieved by solving for a constant offset correction on the ISS attitude data. In practice, we usually solve for an affine or a quadratic correction rather than just an offset to account for potential other unknown errors, if the number of ground control points allows such correction to be reliable.

The general principle to correct for the absolute geolocation error is to gather ground control points (GCPs) within each scene in order to solve for the missing absolute attitude information. GCPs information are propagated back to the ray-tracing model and a correction model is updated such that error with the GCPs is minimized. In practice, GCPs are gathered automatically using image matching between an ortho-rectified reference and the given rectified EMIT frame with ISS geolocation uncertainty. The general scheme borrows from and is illustrated in Figure 11:

1. Generate a ortho-rectified EMIT image based on the EMIT camera model initially located with ISS pointing and position information.
2. Apply image algorithm between the EMIT rectified image and the accurately geolocated reference Landsat imagery. Image matching is performed using Fourier phase correlation, as described in (Bryant et al., 2004, Leprince, et al., 2007).
3. Filter out mismatches and produce GCPs.
4. Use GCPs to update EMIT projection model.
5. Potentially iterate steps 1-4.
6. Deliver corrected geolocation information for all image pixels for the EMIT scene.

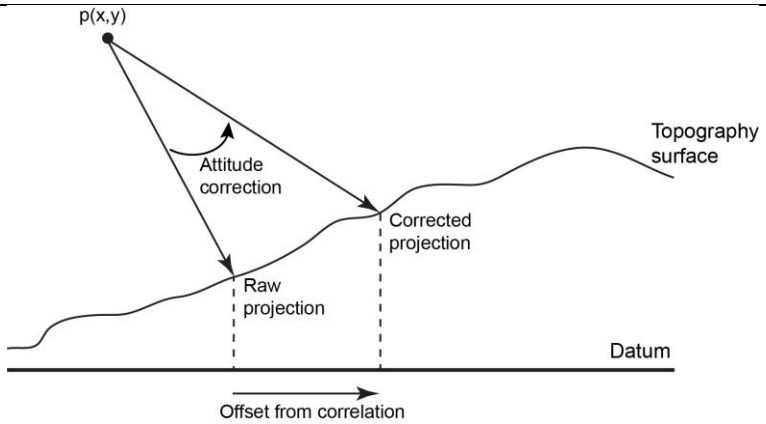

Figure 11: General scheme to update EMIT absolute attitude uncertainty

The geolocation accuracy after correction should match the level of accuracy given by the image matching. Fourier phase correlation methods have demonstrated matching accuracy to be better than 1/10 of the pixel size.

For image matching purpose, EMIT covers the same wavelength range and can be convolved to the Landsat bands and can therefore easily be matched to the Landsat global reference. This offers a high confidence of good quality image matching. The Landsat reference imaging has excellent absolute geolocation accuracy. EMIT imagery matching is expected to achieve a geolocation accuracy on the order of 50m.

Geolocation Corrections Interpolation/Extrapolation

It is frequently the case that for a particular scene image matching with the global ortho-base cannot be performed. This might occur because scenes are over water, or the scenes are cloudy, or we just have scenes without a lot of features to match. To accommodate this, we look at all scenes in the orbit. If we successfully match any of the scenes, then corrections from that scene can be applied to all the scenes in the orbit (see Figure 12). This works because although the ISS attitude knowledge error can be large, it is slowly varying.

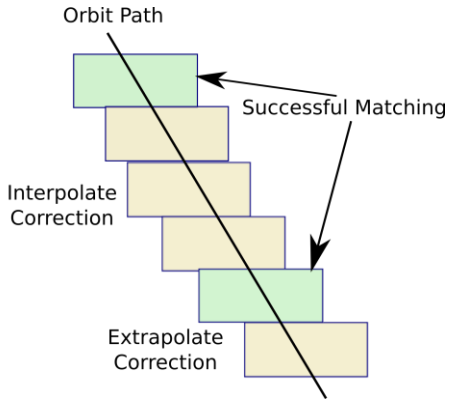

Figure 12 Interpolating/Extrapolating Corrections

4.4 Practical considerations

The radiometric code is implemented in C, and operates independently on single frames of data read and written one at a time. The operations are all computationally fast and tractable. The largest single operations are the corrections for stray spectral and spatial response, which involve multiplication of spectra and rows by matrices sized 328x328 and 1280x1280 respectively. Even these are tractable. All other data dependencies are instrument parameters set during commissioning

(such as the pedestal shift coefficients in Equation 3 above) are encoded in the software version directly using software best practice for holding data; they are not ever expected to change. They are reported in the detatched ASCII header files as independent fields.

5. Output Data

While the EMIT input and output data products delivered to the DAAC use their formatting conventions, the system operates internally on data products stored as binary data cubes with detatched human-readable ASCII header files. The precise formatting convention adheres to the ENVI standard, which can be accessed (Dec. 2019) at https://www.harrisgeospatial.com/docs/ENVIHeaderFiles.html. The header files all consist of data fields in equals-sign-separated pairs, and describe the layout of the file. The output of the L1b radiometric stage output is simply:

1. **Calibrated Spectral Radiance** representing incident illumination at the sensor in μW nm^{-1} cm^{-2} sr^{-1} as measured by the EMIT instrument.

The radiance data is stored in Band-Interleaved-by-Line(BIL), with size [rows x channels x columns], in IEEE little endian single-precision floating point. A detatched header file holds information on wavelength calibration, channel response full width at half maximum, and map projection information, following the header convention above. The geolocation stage has multiple output files:

1. **Corrected Spacecraft Attitude and Ephemeris (ATT),** contains the uncorrected Broadcast Ancillary Data (BAD) ephemeris and attitude quaternions from the ISS, and the data after correction by the geolocation process.
2. **L1B Pixel Location File (LOC)**, a file giving the latitude, longitude and height for each EMIT radiance pixel
3. **L1B Observation Geometric File (OBS)**, various derived parameters such as view angle, solar angle, surface slope and aspect.
4. **L1B Geographic Lookup Table (GLT),** geocorrected product with a fixed pixel size projected into a Geographic projection that contains the information about which original pixel occupies which output pixel in the final product.
5. **L1B Spectral Radiance Quicklook,** red, green, and blue (RGB) composite map-projected image in PNG format generated from the L1B radiance spectral cube.
6. **Level 1B Spectral Radiance KMZ File**, red, green, and blue (RGB) composite map-projected image in KMZ format generated from the L1B radiance spectral cube.

Table 4 Below enumerates all output products.

Instrument Output File	Format	Interpretation
Radiance	[rows x bands x columns] float 32, BIL interleave with detached ASCII header	Radiance at sensor in μW nm^{-1} cm^{-2} sr^{-1}
Corrected Spacecraft Attitude and Ephemeris (ATT),	netCDF	The uncorrected Broadcast Ancillary Data (BAD) ephemeris and attitude quaternions from the ISS, and the data after correction by the geolocation process.
L1B Pixel Location File (LOC),	ENVI	Various derived parameters such as view angle, solar angle, surface slope and aspect.
L1B Geographic Lookup Table (GLT),	ENVI	Geocorrected product with a fixed pixel size projected into a Geographic projection that contains the information about which original pixel occupies which output pixel in the final product.
L1B Spectral Radiance Quicklook	PNG	Red, green, and blue (RGB) composite map-projected image in PNG format generated from the L1B radiance spectral cube.

Level 1B Spectral Radiance KMZ File	KMZ	Red, green, and blue (RGB) composite map-projected image in KMZ format generated from the L1B radiance spectral cube.

Table 4: Output files

6. Calibration, uncertainty characterization, and validation

Achieving the EMIT instrument sensitivity rests on a foundation of very accurate instrument calibration. Radiance uncertainty comes from several sources. One is systematic error related to calibration, such as: (1) measurement uncertainties in measurements used for the spectral or radiometric calibration process; (2) modeling error due to algorithm simplifications and approximations, which make them unable to represent the actual spectral and radiometric properties at perfect fidelity; and (3) drift in calibration over time due to degradation. Other uncertainties relate to the measurement noise, which is a random component of each measurement. The measurement noise can be further decomposed into a signal independent portion caused mainly by instrument thermal and electronic state, and a signal dependent portion induced by photon shot noise counting statistics. All uncertainties have some degree of correlation across channels. But for simplicity the EMIT mission characterizes and reports Level 1a radiance uncertainty on a per-channel basis. Systematic uncertainties will be characterized and reported separately through detailed study, but record random measurement noise, written $\sigma_{meas}(\lambda, L)$ directly within the L1a product itself. The model adds known noise sources in quadrature, and accounts for the number of detector readout events added to form each spectrum:

$$\sigma_{meas}(\lambda, L) = \sqrt{\sigma_{shot}(\lambda, L)^2 + \sigma_{dark}(\lambda)^2 + \sigma_{read}^2 + \sigma_{quant}^2} \; / \; \sqrt{n_{read}}$$

Where $\sigma_{shot}(\lambda, L)$ is the standard deviation of photon shot noise, $\sigma_{dark}(\lambda)$ is the dark current contribution, σ_{read} is uncertainty due to readout noise, and σ_{quant} represents truncation-related error due to finite precision storage. We characterize these in advance from laboratory data, and update the model only as needed during the mission. To simplify the data products, we represent the uncertainties above using a simplified functional form, writing the total measurement noise as an independent function of the radiance signal level for each channel. This spectrally-defined function is independent for each acquisition and recorded in the metadata as the three wavelength-indexed functions $\eta_1(\lambda)$, $\eta_2(\lambda)$, and $\eta_3(\lambda)$. The total radiance uncertainty, in noise-equivalent change in radiance units, can then be computed efficiently for any channel as:

$$\sigma_{meas}(\lambda, L) \approx \eta_1(\lambda)\sqrt{\eta_2(\lambda)L(\lambda)} + \eta_3(\lambda) \qquad (13)$$

For simplicity, the uncertainty model presumes measurement noise appears as a Gaussian distribution centered on the true radiance. This is not a perfect representation of the error distribution, but enables easy analytical error propagation in subsequent algorithms.

Radiance data is typically validated in flight by acquiring in-situ measurements of surface and atmosphere conditions, and then predicting the resulting measurement using radiative transfer models (RTMs) such as MODTRAN (Berk et al., 2016; 2016b), or the 6S code used in routines like ATREM (Thompson et al., 2019). An example appears in Figure 6 below, which compares two radiative transfer model predictions over a calibration/validation experiment site using remote data from the AVIRIS-NG instrument (Babu et al., 2019). The left panel illustrates the field validation protocol. The field team deploys handheld spectroradiiometers in a grid pattern subtending a wide area of the playa for a uniform spatial average. They return periodically to a reference standard target, the spectralon panel on the tripod at center. This allows a conversion to absolute reflectance values: the radiance from the playa is ratioed against that of the standard panel. We correct this ratio to account for the Bidirectional Reflectance Function of the spectralon target at the given solar

zenith, and the intrinsic reflectance signature of the spectralon itself. The result is a reflectance measurement which is combined with in-situ sunphotometer estimates of water vapor and Aerosol Optical Thickness. Optionally, we fit the atmospheric parameters dynamically using iterative retrieval techniques such those in the EMIT Level 2A reflectance estimates (Thompson et al., 2018b). Either way, the result is a prediction for the radiance at sensor which can be compared directly to the measurement and check both absolute and relative calibration.

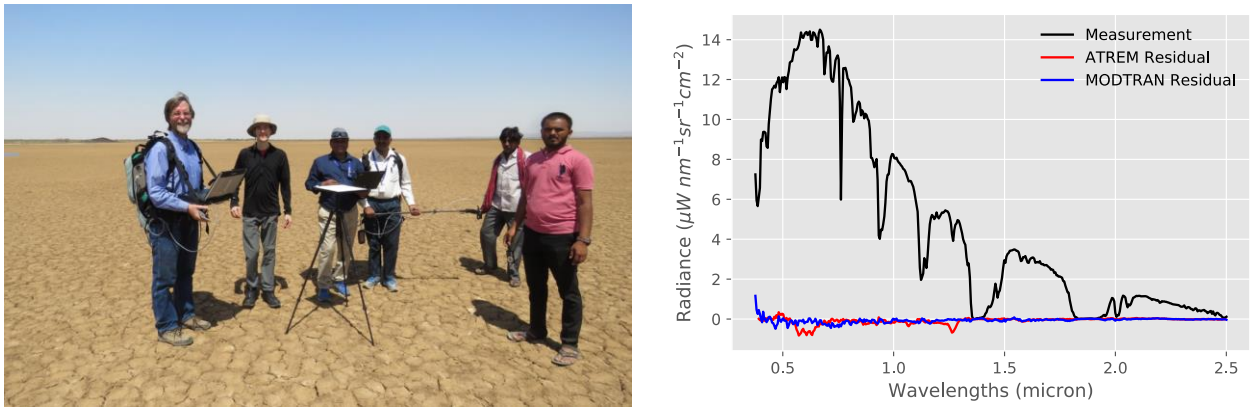

Figure 6: Field validation procedure at Desalpar Playa, India, adapted from Babu et al., (2019). (Left) Field team with in-situ refeerence targets

7. Constraints and Limitations

No constraints or limitations are imposed on the L1B radiometric products. All delivered data will have undergone quality control and should be considered valid calibrations up to the reported uncertainties in input parameters. Unanticipated data corruption due to factors outside the modeling, if discovered, will be reported in peer reviewed literature and/or addenda to this ATBD.

References

Babu, K. N., Mathur, A. K., Thompson, D. R., Green, R. O., Patel, P. N., Prajapati, R. P., ... & Helmlinger, M. C. (2019). An empirical comparison of calibration and validation methodologies for airborne imaging spectroscopy. *CURRENT SCIENCE*, *116*(7), 1101.

Chapman, J., Thompson, D. R., Helmlinger, M. C., Eastwood, M. L., Bue, B. D., Geier, S., Green, R. O., Lundeen, S. R., Olson-Duvall, W. (2019). Spectral and Radiometric Calibration of the Next Generation Airborne Visible Infrared Spectrometer (AVIRIS-NG). *Remote Sensing*, 11(18), 2129.

Berk, A., et al. (2016). Algorithm Theoretic Basis Document (ATBD) for Next Generation MODTRAN®. Spectral Sciences, Inc.: Burlington, MA, USA.

Berk, A., J. van den Bosch, F. Hawes, T. Perkins, P.F. Conforti, G.P. Anderson, R.G. Kennett, P.K. Acharya (2016b). MODTRAN®6.0.0 User's Manual (revision 5). Spectral Sciences, Inc.: Burlington, MA, USA. SSI-TR-685.

Green, R. O., Eastwood, M. L., Sarture, C. M., Chrien, T. G., Aronsson, M., Chippendale, B. J., ... & Olah, M. R. (1998). Imaging spectroscopy and the airborne visible/infrared imaging spectrometer (AVIRIS). *Remote sensing of environment*, *65*(3), 227-248.

Green, R. O., et al. (2011), The Moon Mineralogy Mapper (M^3) imaging spectrometer for lunar science: Instrument description, calibration, on-orbit measurements, science data calibration and on-orbit validation, *J. Geophys. Res.*, 116, E00G19, doi:10.1029/2011JE003797.

Murchie, S. L., Arvidson, R. E., Bedini, P., Beisser, K., Bibring, J. P., Bishop, J., and others and Des Marais, D. (2004). CRISM (compact reconnaissance imaging spectrometer for Mars) on MRO (Mars reconnaissance orbiter). *Instruments, Science, and Methods for Geospace and Planetary Remote Sensing* 5660, 66-77.

Thompson, D. R., Gao, B. C., Green, R. O., Roberts, D. A., Dennison, P. E., & Lundeen, S. R. (2015). Atmospheric correction for global mapping spectroscopy: ATREM advances for the HyspIRI preparatory campaign. *Remote Sensing of Environment*, *167*, 64-77.

Thompson, D. R., Boardman, J. W., Eastwood, M. L., Green, R. O., Haag, J. M., Mouroulis, P., & Van Gorp, B. (2018). Imaging spectrometer stray spectral response: In-flight characterization, correction, and validation. *Remote Sensing of Environment*, *204*, 850-860.

Thompson, D. R., Natraj, V., Green, R. O., Helmlinger, M. C., Gao, B. C., & Eastwood, M. L. (2018b). Optimal estimation for imaging spectrometer atmospheric correction. *Remote sensing of environment*, *216*, 355-373.

Thompson, D. R., Guanter, L., Berk, A., Gao, B. C., Richter, R., Schläpfer, D., & Thome, K. J. (2019). Retrieval of atmospheric parameters and surface reflectance from visible and shortwave infrared imaging spectroscopy data. *Surveys in Geophysics*, *40*(3), 333-360.